

ACCEPTED MANUSCRIPT

## Phase-contrast breast CT: the effect of propagation distance

To cite this article before publication: Luca Brombal *et al* 2018 *Phys. Med. Biol.* in press <https://doi.org/10.1088/1361-6560/aaf2e1>

### Manuscript version: Accepted Manuscript

Accepted Manuscript is “the version of the article accepted for publication including all changes made as a result of the peer review process, and which may also include the addition to the article by IOP Publishing of a header, an article ID, a cover sheet and/or an ‘Accepted Manuscript’ watermark, but excluding any other editing, typesetting or other changes made by IOP Publishing and/or its licensors”

This Accepted Manuscript is © **2018 Institute of Physics and Engineering in Medicine.**

During the embargo period (the 12 month period from the publication of the Version of Record of this article), the Accepted Manuscript is fully protected by copyright and cannot be reused or reposted elsewhere.

As the Version of Record of this article is going to be / has been published on a subscription basis, this Accepted Manuscript is available for reuse under a CC BY-NC-ND 3.0 licence after the 12 month embargo period.

After the embargo period, everyone is permitted to use copy and redistribute this article for non-commercial purposes only, provided that they adhere to all the terms of the licence <https://creativecommons.org/licenses/by-nc-nd/3.0>

Although reasonable endeavours have been taken to obtain all necessary permissions from third parties to include their copyrighted content within this article, their full citation and copyright line may not be present in this Accepted Manuscript version. Before using any content from this article, please refer to the Version of Record on IOPscience once published for full citation and copyright details, as permissions will likely be required. All third party content is fully copyright protected, unless specifically stated otherwise in the figure caption in the Version of Record.

View the [article online](#) for updates and enhancements.

Note

## Phase-contrast breast CT: the effect of propagation distance

Luca Brombal<sup>1,2</sup>, Sandro Donato<sup>1,2</sup>, Diego Dreossi<sup>3</sup>, Fulvia Arfelli<sup>1,2</sup>, Deborah Bonazza<sup>4</sup>, Adriano Contillo<sup>5,6</sup>, Pasquale Delogu<sup>7,8</sup>, Vittorio Di Trapani<sup>7,8</sup>, Bruno Golosio<sup>9,10</sup>, Giovanni Mettivier<sup>11,12</sup>, Piernicola Oliva<sup>13,10</sup>, Luigi Rigon<sup>1,2</sup>, Angelo Taibi<sup>5,6</sup> and Renata Longo<sup>1,2</sup>

<sup>1</sup>Department of Physics, University of Trieste, Via A. Valerio 2, 34127 Trieste, Italy

<sup>2</sup>INFN Division of Trieste, Via A. Valerio 2, 34127 Trieste, Italy

<sup>3</sup>Elettra-Sincrotrone Trieste S.C.p.A, 34149 Basovizza Trieste, Italy

<sup>4</sup>Department of Medical Science, Cattinara Hospital, University of Trieste, Strada di Fiume 447, 34149 Trieste, Italy

<sup>5</sup>Department of Physics and Earth Science, University of Ferrara, Via Savonarola 9, 44121 Ferrara, Italy

<sup>6</sup>INFN Division of Ferrara, via Saragat 1, 44122 Ferrara, Italy

<sup>7</sup>Department of Physical sciences, Earth and Environment, University of Siena, Strada Laterina 8, 53100 Siena, Italy

<sup>8</sup>INFN Division of Pisa, Largo Bruno Pontecorvo 3, 56127 Pisa, Italy

<sup>9</sup>Department of Physics, University of Cagliari, Monserrato-Sestu, I-09042 Monserrato, Italy

<sup>10</sup>INFN Division of Cagliari, Monserrato-Sestu, I-09042 Monserrato, Italy

<sup>11</sup>Department of Physics, University of Napoli Federico II, Via Cinthia, 80126 Fuorigrotta, Napoli, Italy

<sup>12</sup>INFN Division of Napoli, Via Cinthia, 80126 Fuorigrotta, Napoli, Italy

<sup>13</sup>Department of Chemistry and Pharmacy, University of Sassari, Via Vienna, 07100 Sassari SS, Italy

E-mail: [luca.brombal@ts.infn.it](mailto:luca.brombal@ts.infn.it)

July 2018

**Abstract.** X-ray phase imaging has the potential to dramatically improve soft tissue contrast sensitivity, which is a crucial requirement in many diagnostic applications such as breast imaging. In this context, a program devoted to perform *in-vivo* phase-contrast synchrotron radiation breast computed tomography is ongoing at the Elettra facility (Trieste, Italy). The used phase-contrast technique is the propagation-based configuration, which requires a spatially coherent source and a sufficient object-to-detector distance. In this work the effect of this distance on image quality is quantitatively investigated scanning a large breast surgical specimen at 3 object-to-detector distances (1.6, 3, 9 m) and comparing the images both before and after applying the phase-retrieval procedure. The sample is imaged at 30 keV with a 60  $\mu\text{m}$  pixel pitch CdTe single-photon-counting detector, positioned at a fixed distance of 31.6 m from the source. The detector fluence is kept constant for all acquisitions. The study shows that, at the largest distance, a 20-fold SNR increase can be obtained by

1  
2  
3  
4  
5 43 applying the phase-retrieval procedure. Moreover, it is shown that, for phase-retrieved  
6 44 images, changing the object-to-detector distance does not affect spatial resolution while  
7 45 boosting SNR (4-fold increase going from the shortest to the largest distance). The  
8 46 experimental results are supported by a theoretical model proposed by other authors,  
9 47 whose salient results are presented in this paper.

10  
11  
12  
13  
14 48 Submitted to: *Phys. Med. Biol.*

## 15 16 17 49 **1. Introduction**

18  
19 50 X-ray breast imaging is an extremely demanding task since high contrast sensitivity,  
20 51 high spatial resolution and low delivered dose are required. In this context, x-  
21 52 ray phase-contrast-imaging is a powerful tool to dramatically enhance soft tissues  
22 53 contrast sensitivity without increasing dose. The advantage of phase-contrast imaging  
23 54 over the conventional absorption imaging is based on the fact that, considering soft  
24 55 tissues and energies in the range 10 – 100 keV, the decrement from unity ( $\delta$ ) of the  
25 56 refraction index ( $n$ ), responsible for phase effects, is about 3 orders of magnitude  
26 57 higher than the absorption term ( $\beta$ ), used in the conventional radiology (Rigon 2014).  
27 58 Several approaches exist to transform the object-induced phase shift into intensity  
28 59 modulations on the detector: interferometric (e.g., gratings), analyzer-based, edge-  
29 60 illumination and free-space-propagation techniques are in use with synchrotron and,  
30 61 in some cases, conventional sources (Bravin et al. 2012, Rigon 2014). From the  
31 62 experimental point of view, the single-shot free-space propagation-based technique  
32 63 is the easiest to implement since it only requires to increase the object-to-detector  
33 64 distance without using optical elements or multi-exposure acquisition. On the contrary,  
34 65 propagation-based imaging has more stringent requirements on the x-ray source spatial  
35 66 coherence and detector spatial resolution with respect to other techniques (e.g., gratings,  
36 67 edge illumination) (Pfeiffer et al. 2006, Olivo & Speller 2007). Images acquired with  
37 68 the propagation-based technique show an enhanced contrast in the tissue interfaces  
38 69 (i.e., edge-enhancement), which in the ray-optical approximation is proportional to the  
39 70 Laplacian of the object-induced phase-shift (Peterzol et al. 2005). The edge-enhanced  
40 71 images can be processed by applying a phase-retrieval (PhR) algorithm which allows,  
41 72 under certain approximations, to recover the induced phase-shift (Burvall et al. 2011). In  
42 73 this work the PhR algorithm based on the homogeneous transport of intensity equation  
43 74 proposed by Paganin and co-workers in 2002 is used (Paganin et al. 2002). In fact,  
44 75 the combined effect of free-space propagation and PhR is to increase the image signal-  
45 76 to-noise ratio (SNR) preserving spatial resolution and, far from sharp interfaces where  
46 77 edge-enhancement is present, contrast (Gureyev et al. 2017).

47 78 Along with phase effects, breast imaging can also take advantage of 3D techniques,  
48 79 such as breast tomosynthesis and breast CT (BCT), which overcome the superposition of  
49 80 the structures inherent in planar imaging potentially hindering the detection of massive

lesions. At present, the development of BCT systems is a hot topic for several research groups and companies, the main challenge being the trade-off between spatial resolution and delivered dose (Sechopoulos 2013, Sarno et al. 2015, Rößler et al. 2017, Kalender et al. 2017).

In this context, the SYRMA-3D (synchrotron radiation for mammography) collaboration aims to set-up the first clinical study of phase-contrast synchrotron radiation BCT at the Elettra synchrotron facility (Trieste, Italy) and promising results on breast specimens have been recently obtained (Longo et al. 2016, Brombal et al. 2018a, Donato et al. 2018).

In this work, the effect of the propagation distance on the image quality, based on scans of total mastectomy specimen acquired at 3 propagation distances, is discussed. Specifically, both the effects of propagation distance and PhR on image metrics as signal-to-noise-ratio, contrast and spatial resolution are reported and compared with a theoretical model proposed by Gureyev, Nesterets and collaborators (Gureyev et al. 2017, Nesterets & Gureyev 2014), which is briefly described in the next section. A major improvement in signal-to-noise ratio at longer propagation distances and at a constant spatial resolution is experimentally demonstrated.

## 2. Materials and methods

### 2.1. Theoretical model

Let us consider an object positioned at a distance  $R_1$  from a monochromatic point x-ray source and at a distance  $R_2$  from a 1D detector (the extension to a 2D detector is straightforward). We further suppose that the incident scalar electromagnetic wave obeys to the homogeneous transport of intensity equation (TIE-hom), so that the intensity at the detector plane ( $I_{R_2}(x)$ , with  $x$  the pixel coordinate) is:

$$I_{R_2}(x) \simeq \left[1 - \sigma^2 \nabla_x^2\right] I_0(x) \quad , \quad (1)$$

$I_0(x)$  being the transmitted intensity in the object plane while  $\sigma^2 = \gamma R' \lambda / (4\pi)$  accounts for the (effective) propagation distance  $R' = (R_1 R_2) / (R_1 + R_2)$ , for the x-ray wavelength  $\lambda$  and for the proportionality factor between the refraction and absorption properties of an interface between 2 materials  $\gamma = (\delta_2 - \delta_1) / (\beta_2 - \beta_1)$  (Gureyev et al. 2017). It is worth noticing that, along with its validity conditions, equation 1 implies that the image recorded at a given distance from the object will be similar to the (absorption) contact plane image (i.e., at a null propagation distance) apart from the object's interfaces, where the Laplacian of the intensity is expected to be significantly different from zero. Therefore, within uniform regions of the images (i.e., far from sharp details), neither the detected signal nor the noise are expected to change significantly upon the propagation process. On the contrary, the spatial resolution improves in the free-space propagation. This can be qualitatively understood considering that the (phase) contrast is increased close to sharp interfaces (i.e., where the Laplacian is not negligible), hence the high spatial frequencies are boosted. The quantitative demonstration of the spatial resolution

1  
2  
3  
4  
5  
6  
7  
8  
9  
10  
11  
12  
13  
14  
15  
16  
17  
18  
19  
20  
21  
22  
23  
24  
25  
26  
27  
28  
29  
30  
31  
32  
33  
34  
35  
36  
37  
38  
39  
40  
41  
42  
43  
44  
45  
46  
47  
48  
49  
50  
51  
52  
53  
54  
55  
56  
57  
58  
59  
60

120 improvement associated to free-space propagation imaging can be found in (Gureyev  
121 et al. 2017). Once the propagation image has been collected, the phase-retrieved image  
122 is obtained by inverting the equation 1. In practice, this is accomplished by convolving  
123 the image with a low-pass filter which, in the spatial frequency domain ( $u$ ), can be  
124 described as (Brombal et al. 2018a):

$$H(u) = [1 + 4\pi^2\sigma^2u^2]^{-1} \quad . \quad (2)$$

125  
126 From the noise reduction perspective, the phase-retrieval filter has nothing special since  
127 any low-pass filter would reduce noise enhancing the SNR. Anyway, the peculiarity of  
128 the phase-retrieval procedure, applied along with the free-space propagation technique,  
129 is that it restores the resolution that would have been observed in the contact plane  
130 image while improving the SNR. This means that, once the phase retrieval has been  
131 applied, the spatial resolution of the image is the same at all propagation distances,  
132 except for magnification effects. In addition, considering flat portions of the image (i.e.,  
133 far from sharp interfaces), phase retrieval does not modify the image contrast. This  
134 can be understood considering that, in practice, phase retrieval acts as a low pass filter,  
135 thus not altering the large area contrast of the image (Gureyev et al. 2017, Kitchen  
136 et al. 2017). Moreover, the fact that large area contrast is not affected by the phase-  
137 retrieval procedure can also be understood from a physical perspective. In fact, in the  
138 analytical derivation of the phase-retrieval formula it is assumed that absorption and  
139 phase properties are proportional throughout the object, thus, far from interfaces, large  
140 area contrast is not expected to vary (Paganin et al. 2002, Burvall et al. 2011).

141 If both phase-retrieval and tomographic reconstruction process are considered, it  
142 can be demonstrated that the SNR gain associated to the application of phase retrieval  
143 in the tomographic image is expected to be (Nesterets & Gureyev 2014):

$$SNR_{gain}(A) = \left[ (8/3\pi) \frac{A^2}{\ln(A) - 1} \right]^{1/2} \quad , \quad (3)$$

144  
145 being  $A = \sigma^2/(16h'^2)$  a dimensionless parameter accounting for the object composition,  
146 irradiation geometry, beam energy (all described by  $\sigma$ ) and the detector effective pixel  
147 size  $h' = h/M$ , where  $h$  is the physical pixel size and  $M = (R_1 + R_2)/R_2$  the magnification  
148 factor. To obtain this result the detector is assumed to be ideal, i.e., with  $MTF = 1$   
149 up to the Nyquist frequency. The equation 3 is the central result of the model and,  
150 as a first approximation, it implies that the SNR gain increases almost linearly with  
151 the propagation distance and with the inverse of the square of the effective pixel size.  
152 Considering realistic parameters in terms of energy (tens of keV), propagation distance  
153 (meters) and pixel size (less than 100  $\mu m$ ), the expected SNR gain is between 1 and 2  
154 orders of magnitude with respect to conventional imaging (Kitchen et al. 2017).

## 155 2.2. Experimental setup and sample

156 The images are acquired at the SYRMEP beamline at Elettra (Tromba et al. 2010).  
157 The x-ray beam is produced by one storage ring bending magnet and the energy is

1  
2  
3  
4  
5 selected in the range 8.5 - 40 keV by means of a Si(111) double-crystal monochromator,  
6 providing an energy resolution of 0.1%. The beam's cross section at the detector  
7 is 220 (horizontal)  $\times$  4 mm<sup>2</sup> (vertical, Gaussian shape, FWHM) while the source-to-  
8 detector distance is kept at 31.6 m for all measurements. Images are collected at  
9 30 keV positioning the sample at 3 different object-to-detector distances, 1.6, 3 and  
10 9 m, respectively. The laminar shape of the beam, along with long object-to-detector  
11 distances, allows to work in a scatter-free geometry without the need of anti-scattering  
12 grids (Brombal et al. 2018a). To be consistent with the notation of the model presented  
13 in the previous section, the propagation distance ( $R'$ ) is defined as the object-to-detector  
14 distance scaled by the magnification factor. Given that the magnifications at the 3  
15 sample positions are 1.05, 1.1 and 1.4, the propagation distances will be 1.5, 2.7 and  
16 6.4 m, respectively. It is worth noticing that, especially at high magnifications, the  
17 actual finite dimension of the source should be taken into account since it contributes  
18 to the overall image blurring, thus reducing the spatial resolution (Gureyev et al. 2008).  
19 Anyway, in this work small magnifications (up to 1.4) are used and the detector spatial  
20 resolution is similar to the source size ( $\sim 100 \mu\text{m}$ ) (SYRMEP 2016), therefore making  
21 the source size contribution to the image blurring (as a first approximation) negligible.

22 Each scan is performed in 40 seconds, collecting the projections over 180 deg with  
23 a rotation speed of 4.5 deg sec<sup>-1</sup>. The dose, expressed as mean glandular dose (MGD),  
24 is evaluated by multiplying the air kerma at the patient position (i.e., 1.6 m object-to-  
25 detector distance) by a conversion factor accounting for breast size and glandularity,  
26 derived from an ad-hoc developed Monte Carlo simulation based on a GEANT4  
27 code (Mettivier et al. 2015, Fedon et al. 2015). In this study, the delivered MGD at  
28 the shortest propagation distance was 25 mGy. At larger distances, since the fluence on  
29 the detector was kept roughly constant, the delivered dose was slightly increased ( $\sim 5\%$   
30 higher at 3 m and  $\sim 30\%$  higher at 9 m) due to x-ray attenuation in air. In *in-vivo*  
31 applications, this issue can easily be overcome by positioning a vacuum pipe between  
32 the object and the detector, thus avoiding air attenuation. In addition, as it will be  
33 clear in the next section, it can be argued that air attenuation is largely compensated  
34 by the SNR increase at larger distances, leaving room for the possibility of a major dose  
35 reduction.

36 The sample is a total breast mastectomy containing an epithelial and stromal  
37 sarcomatoid carcinoma. After the formalin fixation and sealing in a vacuum bag,  
38 the sample diameter is of about 12 cm. The Directive 2004/23/EC of the European  
39 Parliament and of the Council of 31 March 2004 on setting standards of quality and  
40 safety for the donation, procurement, testing, processing, preservation, storage and  
41 distribution of human tissues were followed.

42 The images are collected with a CdTe single-photon-counting detector with a 60  $\mu\text{m}$   
43 pixel pitch (Pixirad-8), comprising an array of 8 modules tiling a total surface of  
44 246  $\times$  25 mm<sup>2</sup>, operated in dead-time-free mode at a frame rate of 30 Hz (Bellazzini  
45 et al. 2013, Delogu et al. 2017). Each scan is constituted by 1200 projections which first  
46 undergo an ad-hoc pre-processing procedure (Brombal et al. 2018b) and subsequently are  
47

1  
2  
3  
4  
5  
6  
7  
8  
9  
10  
11  
12  
13  
14  
15  
16  
17  
18  
19  
20  
21  
22  
23  
24  
25  
26  
27  
28  
29  
30  
31  
32  
33  
34  
35  
36  
37  
38  
39  
40  
41  
42  
43  
44  
45  
46  
47  
48  
49  
50  
51  
52  
53  
54  
55  
56  
57  
58  
59  
60

200 phase-retrieved ( $\gamma = 795$ ) and reconstructed via a GPU-based filtered back projection  
201 with a Shepp-Logan filtering (Brun et al. 2015). The value of the retrieval parameter  
202  $\gamma$  has been extracted from a publicly available database (Taylor 2015) considering a  
203 glandular/adipose interface.

### 204 2.3. Image analysis

205 As a first step the SNR of the images prior to the phase retrieval is measured selecting  
206 circular ROIs (4000 pixels each) embedded within tumoral tissue, avoiding sharp edges.  
207 According to the TIE model (equation 1) SNR should not change significantly varying  
208 the propagation distance if no phase-retrieval is applied, being equal to the SNR that  
209 would be observed in the contact plane. To compensate for the beam's magnification,  
210 SNR is normalized to square root of the effective pixel size  $h' = h/M$ , where  $h = 60 \mu\text{m}$   
211 is the physical pixel pitch and  $M$  is the magnification. Moreover, to make up for small  
212 fluence variations in different acquisitions, SNR is also normalized to the square root of  
213 the average number of counts in the detector  $N$ , and defined to be:

$$214 \quad SNR = \frac{\langle I \rangle}{s(I)} \sqrt{\frac{h'_0}{h'}} \sqrt{\frac{N_0}{N}} \quad , \quad (4)$$

215 where  $\langle I \rangle$  is the mean pixel value,  $s(I)$  the standard deviation in the ROI,  $h'_0$  and  
216  $N_0$  are the reference pixel size and number of counts corresponding to the 1.5 m  
217 propagation distance acquisition, respectively. The error associated to the SNR is given  
218 by the standard deviation of 5 SNR measurements performed in non-overlapping ROIs.  
219 SNR is measured also after the application of the phase-retrieval algorithm and a gain  
220 factor is defined as:

$$221 \quad SNR_{gain} = \frac{SNR_{PhR}}{SNR_{noPhR}} \quad . \quad (5)$$

222 Subsequently, the image contrast is measured selecting ROIs both within tumor  
223 (subscript 1) and adipose (subscript 2) regions:

$$224 \quad C = \frac{\langle I_1 \rangle - \langle I_2 \rangle}{\langle I_2 \rangle} \times 100 \quad . \quad (6)$$

225 Since phase retrieval is affecting only image noise while free space propagation is  
226 affecting spatial resolution, the contrast should not change neither with the application  
227 of the phase retrieval, nor varying the propagation distance. As for the SNR, the  
228 error associated to the contrast is given by the standard deviation of 5 contrast values  
229 measured in non-overlapping ROI pairs.

230 The spatial resolution is measured in the phase-retrieved images selecting, for each  
231 distance, 3 line profiles across a sharp fat/tumor interface produced by a surgical cut.  
232 The line profiles are fitted with an *erf* and the FWHM of its derivative is measured.  
233 The spatial resolution is evaluated as the mean value of the 3 FWHMs and the error  
234 is estimated to be the maximum fluctuation around the mean value. According to the  
235 theory, excluding the effect of the magnification, the spatial resolution after the PhR  
236 should not vary by changing the propagation distance since, for each distance, the PhR is

237 expected to produce the same resolution that would have been measured in the contact  
238 plane image. In order to consider only the intrinsic system's spatial resolution, the  
239 FWHM is measured in number of pixels instead of an absolute length.

### 240 3. Results and discussion

241 In figure 1 the reconstructed slices at different propagation distances (1.5, 2.7, 6.4 m)  
242 without (a-c) and with (d-f) the phase retrieval are reported. With the aim of a  
243 visualization allowing a straightforward comparison between images with and without  
244 phase retrieval, all the images have been scaled by a normalization factor such that  
245 the average value of fibroglandular tissues far from interfaces is 1 while air is 0. Since  
246 tissue relaxation occurred and sample repositioning was needed, some morphological  
247 changings (e.g., different position of air gaps within the tissue) are observed at different  
248 propagation distances. Care was taken to ensure the best match at all distances in  
249 the region enclosed by the dashed line of figure 1 (a), where all the measurements are  
250 performed. From the images it can be qualitatively noted that, if no PhR is applied,  
251 no major variation in signal and noise is observed by varying the propagation distance,  
252 except for the sharp interfaces between adipose (dark grey) and tumor or fibroglandular  
253 (bright gray) tissue. On the contrary, increasing the propagation distance, the phase-  
254 retrieved reconstructions are smoother and no spatial resolution degradation is observed.

255 The same effect is reported in a finer detail in figure 2, where a zoom on a sharp  
256 adipose/tumor interface produced by a surgical cut is displayed. Considering the non-  
257 phase retrieved images (a-c) it is clear that the edge-enhancement effect at the interfaces  
258 between the two different tissues is amplified at increasing propagation distances, i.e.,  
259 the high-spatial frequencies are boosted. This can be better visualized in panels (g-  
260 i) reporting line profiles (see dashed line in panels (a-c)) of the non-phase-retrieved  
261 images at increasing propagation distances. Besides the edge-enhancement effect, clearly  
262 visible in panel (i), the profiles show a high level of noise, possibly hampering tissue  
263 differentiation. On the other hand, when the PhR is applied (d-f) the edge appearance  
264 does not change by varying the propagation distance and the edge-contrast is not longer  
265 present. Considering the respective line profiles reported in panels (j-l), a similar edge  
266 sharpness is observed at all distances and, when compared with the non-phase-retrieved  
267 images profiles, the noise level is significantly lower.

268 The quantitative results are reported in table 1. As predicted by the theory  
269 the SNR, calculated according to equation 4, does not vary significantly with the  
270 propagation distance prior to the PhR, while its increase associated with the phase  
271 retrieval is greater than a factor of 20 when considering 6.4 m of propagation distance.  
272 In addition, it must be noted that only little contrast variations (below 3%) are observed  
273 when changing the distance while, at a given position, no significant contrast alterations  
274 are associated to the PhR algorithm whose action is limited to image noise. Furthermore,  
275 considering phase-retrieved images, the FWHM measured in pixel units does not vary  
276 significantly with the propagation distances and, in all cases, was found to be slightly



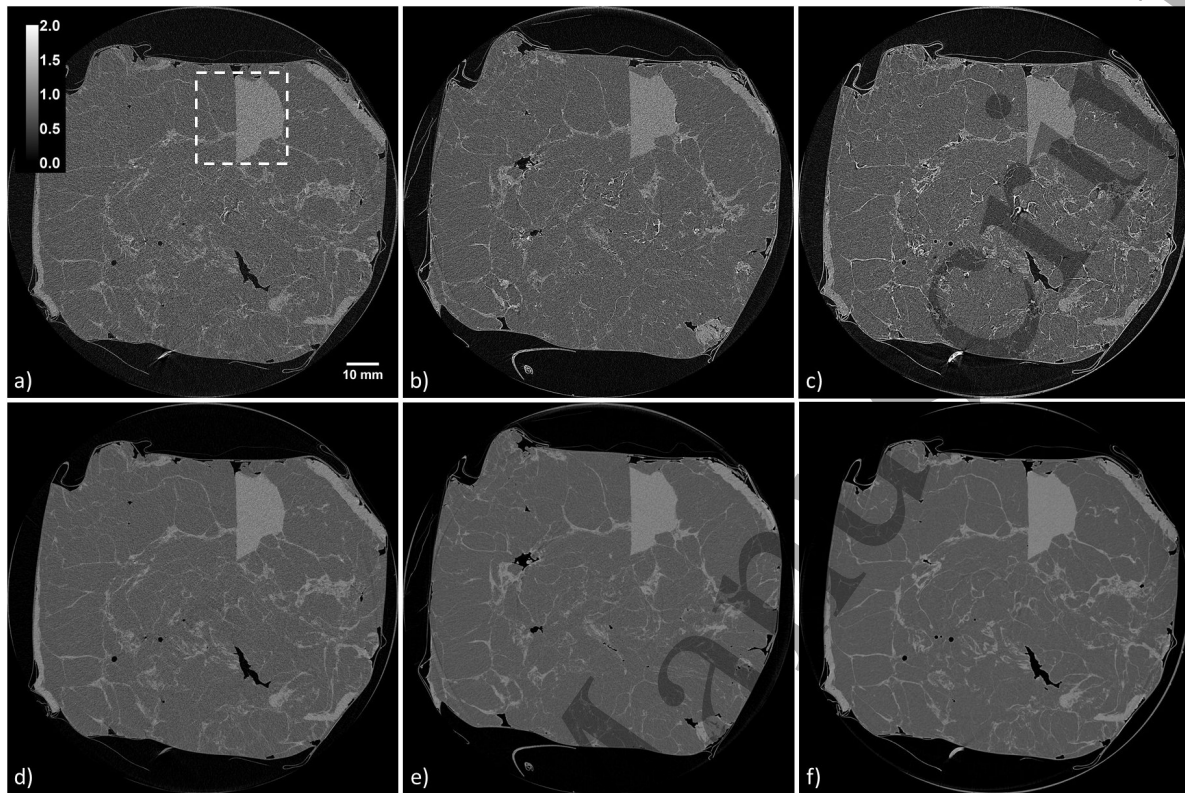


**Figure 1.** Reconstructed slice acquired at propagation distances 1.5 m (a, d), 2.7 m (b, e) and 6.4 m (c, f). Images in the first row (a-c) are reconstructed without PhR, images in the second row (d-f) with PhR. The dashed square in (a) is the zoom region reported in figure 2. After the normalization described in text, images are displayed in a gray scale window ranging from 0 to 2, where 0 is a typical value of air and 1 a typical value of fibroglandular tissue. Morphological variations at different distances are due to sample repositioning and tissue relaxation within the sample holder.

277 higher than 2 pixels ( $\sim 120\mu\text{m}$  on the detector plane). This implies that, taking into  
 278 account the magnification, the actual spatial resolution is improved at longer distances  
 279 (FWHM  $\sim 100\mu\text{m}$ ) at the expense of a smaller field of view.

**Table 1.** Quantitative results. The uncertainty associated to each measure is enclosed between round brackets.

|           | PhR | Distance R' |             |              |
|-----------|-----|-------------|-------------|--------------|
|           |     | 1.52 m      | 2.72 m      | 6.44 m       |
| SNR       | No  | 1.63 (0.02) | 1.63 (0.03) | 1.62 (0.01)  |
|           | Yes | 8.45 (0.13) | 13.3 (0.3)  | 33.8 (0.7)   |
| Contrast  | No  | 32.8 (0.4)  | 30.6 (0.3)  | 33.3 (0.2)   |
|           | Yes | 32.7 (0.2)  | 30.7 (0.1)  | 32.9 (< 0.1) |
| FWHM (px) | Yes | 2.1 (0.5)   | 2.3 (0.3)   | 2.4 (0.2)    |

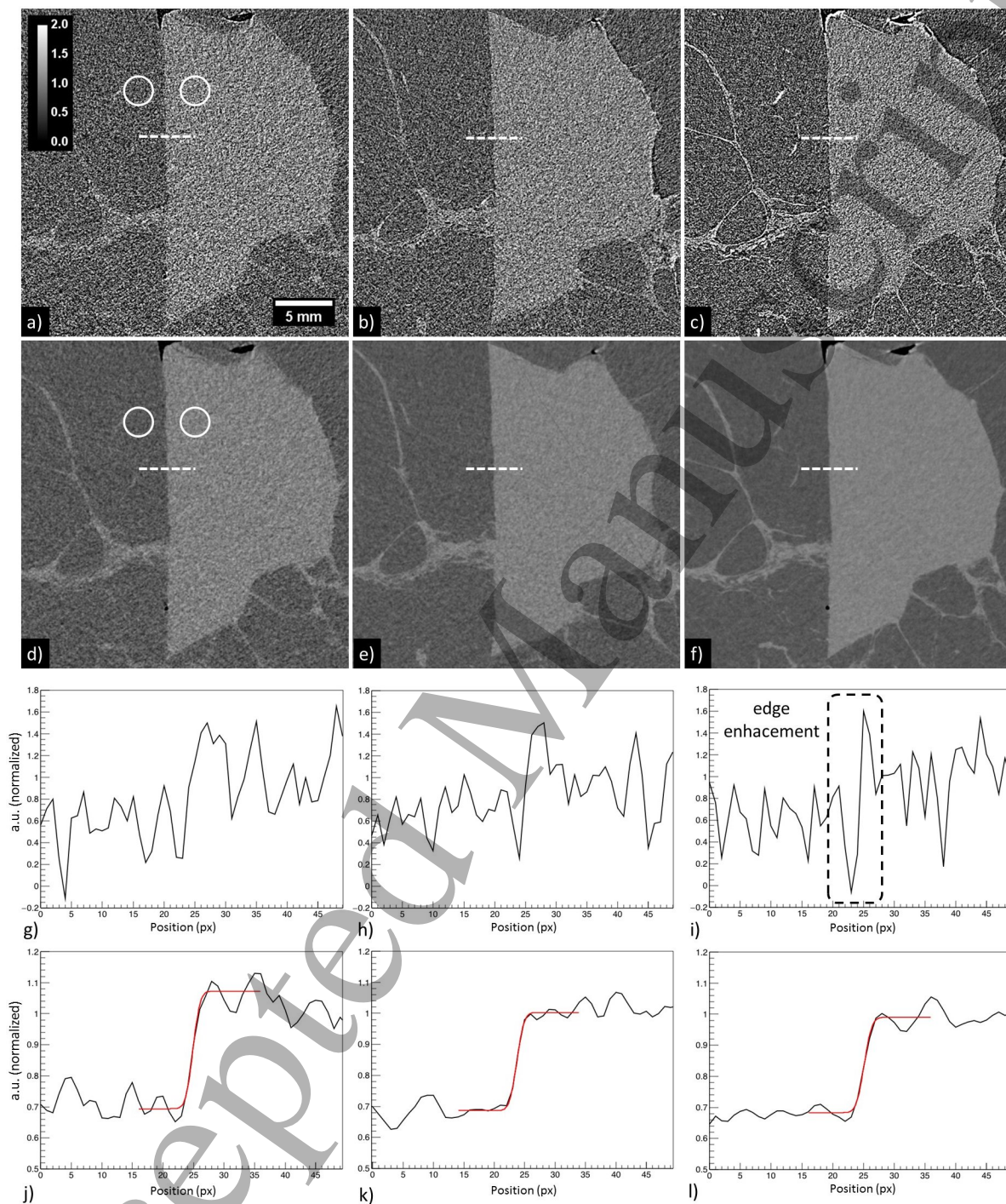


**Figure 2.** Zoomed detail of figure 1 without (a-c) and with (d-f) phase retrieval at increasing propagation distances (from left to right). In panels (g-i) profiles obtained from the dashed lines in (a-c) are reported. In panels (j-l) profiles obtained from the dashed lines in (d-f) are reported along with the *erf* fit (red curve). In (a) and (d) one of the five pairs of circular ROIs used to determine contrast and SNR are displayed as an example.

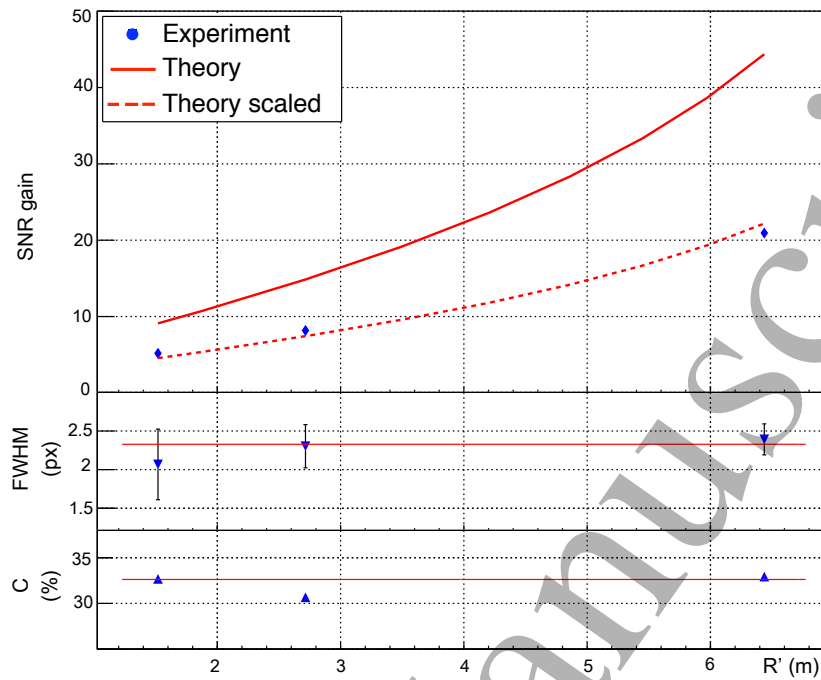


**Figure 3.** Comparison between experimental results (blue points) and theoretical predictions (solid red lines) as a function of the propagation distance. In the top panel the theoretical prediction scaled by a factor of 2 (dashed red line) is also reported. Some error bars are smaller than points.

With the aim of a better data visualization, the measured SNR gain, contrast and spatial resolution concerning the phase-retrieved images (blue points) and the theoretical predictions (solid red lines) are plotted as a function of the propagation distance in figure 3. From the top panel it can be seen that the measured SNR gain is lower than the predicted value at all propagation distances by roughly a factor of 2. This can be simply explained considering that the model assumes an ideal detector with a constant MTF up to the Nyquist frequency, thus constituting in practice an upper limit for the SNR gain when a real detector is considered. Once the theoretical curve is scaled (dashed red line), the experimental points match the theoretical trend. Moreover, comparing phase-retrieved images, a 4-fold increase in SNR can be obtained at 6.4 m with respect to the shortest propagation distance (1.5 m). At the same time, as predicted by the model, the spatial resolution is kept constant at all the distances (central panel) while only little contrast variations are observed (bottom panel).

#### 4. conclusions

This study on a surgical breast specimen indicates that, combining the free-space propagation phase-contrast technique and the phase-retrieval algorithm, it is possible to obtain a major SNR improvement with respect to conventional imaging, at a constant spatial resolution. Specifically, at a fixed detector fluence, the longer propagation

distances provide higher SNR while leaving spatial resolution unaltered. The maximum observed SNR gain associated with the phase-retrieval algorithm is found to be 20 at 6.4 m while, at all propagation distances, the gain is about a factor of 2 smaller than the one predicted by the presented theoretical model which considers an ideal detector with a constant MTF. This means that the trend of the experimental points is consistent with the theory while the quantitative discrepancies should be attributed to the realistic (non-ideal) detector MTF. For the phase retrieved images, the spatial resolution measured across a sharp adipose/tumoral interface, is slightly higher than  $100\mu\text{m}$  at all the propagation distances. In addition, it has been shown that, with the described experimental setup, major contrast variations are not observed neither changing propagation distance nor applying the phase-retrieval. This fact is of great importance in sight of the clinical application of this technique, since the image appearance will look "familiar" to the clinician's eye, who will not need a specific training to read the images. The presented work, where one sample was scanned at a limited number of propagation distances, will be expanded using different samples, propagation distances and including the detector's MTF in the theoretical model. Moreover, the SYRMEP beamline is being re-designed to accommodate larger patient-to-detector distances (1.6 m in the present configuration) to better exploit the advantages of the free-space propagation technique in breast CT clinical applications.

## Acknowledgments

The authors gratefully thank Timur Gureyev and Yakov Nesterets for the fruitful discussion on the theoretical model and Giuliana Tromba for her support in the experimental activities. The authors gratefully acknowledge all the members of the SYRMA-3D project, Elettra-Sincrotrone Trieste SCpA and the Cattinara University Hospital for their support. Sandro Donato is partially supported by Consorzio per la Fisica Trieste.

## References

- Bellazzini, R., Spandre, G., Brez, A., Minuti, M., Pinchera, M. & Mozzo, P. (2013). Chromatic x-ray imaging with a fine pitch cdte sensor coupled to a large area photon counting pixel asic, *Journal of Instrumentation* **8**(02): C02028.
- Bravin, A., Coan, P. & Suortti, P. (2012). X-ray phase-contrast imaging: from pre-clinical applications towards clinics, *Physics in Medicine & Biology* **58**(1): R1.
- Brombal, L., Donato, S., Brun, F., Delogu, P., Fanti, V., Oliva, P., Rigon, L., Di Trapani, V., Longo, R. & Golosio, B. (2018b). Large-area single-photon-counting cdte detector for synchrotron radiation computed tomography: a dedicated pre-processing procedure, *Journal of Synchrotron Radiation* **25**(4).
- Brombal, L., Golosio, B., Arfelli, F., Bonazza, D., Contillo, A., Delogu, P., Donato, S., Mettievier, G., Oliva, P., Rigon, L. et al. (2018a). Monochromatic breast ct: absorption and phase-retrieved images, *Medical Imaging 2018: Physics of Medical Imaging*, Vol. 10573, International Society for Optics and Photonics, p. 1057320.

- 338 Brun, F., Pacilè, S., Accardo, A., Kourousias, G., Dreossi, D., Mancini, L., Tromba, G. & Pugliese,  
339 R. (2015). Enhanced and flexible software tools for x-ray computed tomography at the italian  
340 synchrotron radiation facility elettra, *Fundamenta Informaticae* **141**(2-3): 233–243.
- 341 Burvall, A., Lundström, U., Takman, P. A., Larsson, D. H. & Hertz, H. M. (2011). Phase retrieval in  
342 x-ray phase-contrast imaging suitable for tomography, *Optics express* **19**(11): 10359–10376.
- 343 Delogu, P., Golosio, B., Fedon, C., Arfelli, F., Bellazzini, R., Brez, A., Brun, F., Di Lillo, F., Dreossi,  
344 D., Mettievier, G. et al. (2017). Imaging study of a phase-sensitive breast-ct system in continuous  
345 acquisition mode, *Journal of Instrumentation* **12**(01): C01016.
- 346 Donato, S., Brombal, L., Tromba, G., Longo, R. et al. (2018). Phase-contrast breast-ct: Optimization  
347 of experimental parameters and reconstruction algorithms, *World Congress on Medical Physics  
348 and Biomedical Engineering 2018, IFMBE Proceedings*, Vol. 61, Springer, pp. 109–115.
- 349 Fedon, C., Longo, F., Mettievier, G. & Longo, R. (2015). Geant4 for breast dosimetry: parameters  
350 optimization study, *Physics in Medicine & Biology* **60**(16): N311.
- 351 Gureyev, T. E., Nesterets, Y. I., Kozlov, A., Paganin, D. M. & Quiney, H. M. (2017). On the  
352 unreasonable effectiveness of transport of intensity imaging and optical deconvolution, *JOSA A*  
353 **34**(12): 2251–2260.
- 354 Gureyev, T. E., Nesterets, Y. I., Stevenson, A. W., Miller, P. R., Pogany, A. & Wilkins, S. W. (2008).  
355 Some simple rules for contrast, signal-to-noise and resolution in in-line x-ray phase-contrast  
356 imaging, *Optics express* **16**(5): 3223–3241.
- 357 Kalender, W. A., Kolditz, D., Steiding, C., Ruth, V., Lück, F., Rößler, A.-C. & Wenkel, E.  
358 (2017). Technical feasibility proof for high-resolution low-dose photon-counting ct of the breast,  
359 *European radiology* **27**(3): 1081–1086.
- 360 Kitchen, M. J., Buckley, G. A., Gureyev, T. E., Wallace, M. J., Andres-Thio, N., Uesugi, K., Yagi, N.  
361 & Hooper, S. B. (2017). Ct dose reduction factors in the thousands using x-ray phase contrast,  
362 *Scientific reports* **7**(1): 15953.
- 363 Longo, R., Arfelli, F., Bellazzini, R., Bottigli, U., Brez, A., Brun, F., Brunetti, A., Delogu, P., Di Lillo,  
364 F., Dreossi, D. et al. (2016). Towards breast tomography with synchrotron radiation at elettra:  
365 first images, *Physics in Medicine & Biology* **61**(4): 1634.
- 366 Mettievier, G., Fedon, C., Di Lillo, F., Longo, R., Sarno, A., Tromba, G. & Russo, P. (2015). Glandular  
367 dose in breast computed tomography with synchrotron radiation, *Physics in Medicine & Biology*  
368 **61**(2): 569.
- 369 Nesterets, Y. I. & Gureyev, T. E. (2014). Noise propagation in x-ray phase-contrast imaging and  
370 computed tomography, *Journal of Physics D: Applied Physics* **47**(10): 105402.
- 371 Olivo, A. & Speller, R. (2007). A coded-aperture technique allowing x-ray phase contrast imaging with  
372 conventional sources, *Applied Physics Letters* **91**(7): 074106.
- 373 Paganin, D., Mayo, S., Gureyev, T. E., Miller, P. R. & Wilkins, S. W. (2002). Simultaneous phase  
374 and amplitude extraction from a single defocused image of a homogeneous object, *Journal of  
375 microscopy* **206**(1): 33–40.
- 376 Peterzol, A., Olivo, A., Rigon, L., Pani, S. & Dreossi, D. (2005). The effects of the imaging system  
377 on the validity limits of the ray-optical approach to phase contrast imaging, *Medical physics*  
378 **32**(12): 3617–3627.
- 379 Pfeiffer, F., Weitkamp, T., Bunk, O. & David, C. (2006). Phase retrieval and differential phase-contrast  
380 imaging with low-brilliance x-ray sources, *Nature physics* **2**(4): 258.
- 381 Rigon, L. (2014). x-ray imaging with coherent sources, *Comprehensive Biomedical Physics* **2**: 193–216.
- 382 Rößler, A.-C., Kalender, W., Kolditz, D., Steiding, C., Ruth, V., Preuss, C., Peter, S. C., Brehm,  
383 B., Hammon, M., Schulz-Wendtland, R. et al. (2017). Performance of photon-counting breast  
384 computed tomography, digital mammography, and digital breast tomosynthesis in evaluating  
385 breast specimens, *Academic radiology* **24**(2): 184–190.
- 386 Sarno, A., Mettievier, G. & Russo, P. (2015). Dedicated breast computed tomography: basic aspects,  
387 *Medical physics* **42**(6Part1): 2786–2804.
- 388 Sechopoulos, I. (2013). A review of breast tomosynthesis. part i. the image acquisition process, *Medical*



1  
2  
3  
4  
5 389 *physics* **40**(1).

6 390 SYRMEP (2016). SYRMEP specifications.

7 391 **URL:** [www.elettra.trieste.it/lightsources/elettra/elettra-beamlines/symep/specification.html](http://www.elettra.trieste.it/lightsources/elettra/elettra-beamlines/symep/specification.html)

8 392 Taylor, J. A. (2015). CSIRO TS imaging.

9 393 **URL:** [www.ts-imaging.net/Services/Simple/ICUtilXdata.aspx](http://www.ts-imaging.net/Services/Simple/ICUtilXdata.aspx)

10 394 Tromba, G., Longo, R., Abrami, A., Arfelli, F., Astolfo, A., Bregant, P., Brun, F., Casarin, K., Chenda,  
11 395 V., Dreossi, D. et al. (2010). The symep beamline of elettra: Clinical mammography and bio-  
12 396 medical applications, *AIP Conference Proceedings*, Vol. 1266, AIP, pp. 18–23.

13  
14  
15  
16  
17  
18  
19  
20  
21  
22  
23  
24  
25  
26  
27  
28  
29  
30  
31  
32  
33  
34  
35  
36  
37  
38  
39  
40  
41  
42  
43  
44  
45  
46  
47  
48  
49  
50  
51  
52  
53  
54  
55  
56  
57  
58  
59  
60

Accepted Manuscript